

Journal of Biomedical Optics

BiomedicalOptics.SPIEDigitalLibrary.org

Monitoring of temperature-mediated phase transitions of adipose tissue by combined optical coherence tomography and Abbe refractometry

Irina Y. Yanina
Alexey P. Popov
Alexander V. Bykov
Igor V. Meglinski
Valery V. Tuchin

SPIE.

Irina Y. Yanina, Alexey P. Popov, Alexander V. Bykov, Igor V. Meglinski, Valery V. Tuchin, "Monitoring of temperature-mediated phase transitions of adipose tissue by combined optical coherence tomography and Abbe refractometry," *J. Biomed. Opt.* **23**(1), 016003 (2018), doi: 10.1117/1.JBO.23.1.016003.

Monitoring of temperature-mediated phase transitions of adipose tissue by combined optical coherence tomography and Abbe refractometry

Irina Y. Yanina,^{a,b,*} Alexey P. Popov,^{c,d} Alexander V. Bykov,^{c,d} Igor V. Meglinski,^{c,d,e} and Valery V. Tuchin^{a,b,f,g}

^aSaratov State University, Research-Educational Institute of Optics and Biophotonics, Saratov, Russia

^bTomsk State University, Interdisciplinary Laboratory of Biophotonics, Tomsk, Russia

^cUniversity of Oulu, Optoelectronics and Measurement Techniques Research Unit, Oulu, Finland

^dITMO University, Terahertz Biomedicine Laboratory, St. Petersburg, Russia

^eIrkutsk State University, Institute of Biology, Irkutsk, Russia

^fITMO University, Laboratory of Femtomedicine, St. Petersburg, Russia

^gInstitute of Precision Mechanics and Control of the Russian Academy of Sciences, Laboratory of Laser Diagnostics of Technical and Living Systems, Saratov, Russia

Abstract. Observation of temperature-mediated phase transitions between lipid components of the adipose tissues has been performed by combined use of the Abbe refractometry and optical coherence tomography. The phase transitions of the lipid components were clearly observed in the range of temperatures from 24°C to 60°C, and assessed by quantitatively monitoring the changes of the refractive index of 1- to 2-mm-thick porcine fat tissue slices. The developed approach has a great potential as an alternative method for obtaining accurate information on the processes occurring during thermal lipolysis. © 2018 Society of Photo-Optical Instrumentation Engineers (SPIE) [DOI: 10.1117/1.JBO.23.1.016003]

Keywords: adipose tissue; heating; refractive index; lipolysis; phase transition; Abbe refractometry; optical coherence tomography. Paper 170536PRR received Aug. 16, 2017; accepted for publication Dec. 12, 2017; published online Jan. 2, 2018.

1 Introduction

Monitoring of temperature-mediated phase transitions in biological tissues is an acute problem in the field of laser applications in biology and medicine.^{1,2} This is due to the fact that most of the laser medical technologies rely on thermal effects.³ The laser-tissue thermal interaction, therefore, has been receiving more and more attention in recent years.^{4,5} In particular, designing of optical methods for selective non- or minimally invasive diagnostics and reduction of body fat requires robust technologies to monitor condition of adipose tissue (AT).⁶⁻¹⁵

AT is a multicomponent tissue¹⁶ with constituents presented in Fig. 1. Fats within a lipid droplet in an adipocyte are typically represented by triglyceride (TG) mixtures.¹⁷ TGs are neutral fat molecules made up of three fatty acids connected to one glycerol molecule via the ester. Fatty acids are usually derived from TGs or phospholipids, known as “free” fatty acids (FFAs).^{16,17}

Measurements of the temperature-dependence of the refractive index (RI) can be used for the detection of phase transitions in the AT.^{21,22} The knowledge of thermal response of RI of AT including increments and phase transitions is important for getting a more accurate information on fat cell destruction pathways at laser heating¹¹⁻¹³ or cell lipolysis induced by a low-level laser therapy.¹⁴ There are not many studies on RI of AT, especially in the course of tissue heating, available in the literature.^{9,23-31} Therefore, in this study, the temperature dependence of RI of AT samples has been examined utilizing a combined use of optical coherence tomography (OCT) and Abbe refractometry aiming to quantify RI temperature increment

and lipid phase transitions with the goal to propose an alternative method for objective indication of processes taking place during fat cell destruction/lipolysis. In general, these studies can be useful for improvement in therapeutic protocols based on thermally induced fat cell lipolysis, including laser therapy for body contouring and spot fat reduction and photochemotherapy of cancer patients.¹¹⁻¹⁵

2 Materials and Methods

2.1 Brief Review of Adipose Tissue Properties

Table 1 shows data for RI of ATs measured by different methods and for different body sites in humans and animals.

The AT is characterized by a relatively low temperature and a few melting points that can significantly affect kinetics of the heating of the fat-bearing tissue. The lower fat melting point is caused by a higher content of unsaturated fatty acids, which includes the complex mixtures of TGs. These mixtures do not have a single melting point as the separate compounds.³² The fat crystals can be characterized at the microscopic level (i.e., shape, size, and orientation of crystals in lipid droplets) and at the molecular level (i.e., organization of TGs in lamellar structures of various thicknesses, correspondence to various polymorphic forms, etc.). Within the 24°C to 60°C temperature range, different lipid components of the AT undergo several phase transitions associated with the multicomponent lipid content of fat cells (Tables 2 and 3).^{16,33,34} Detection of such phase

*Address all correspondence to: Irina Yu. Yanina, E-mail: irina-yanina@list.ru

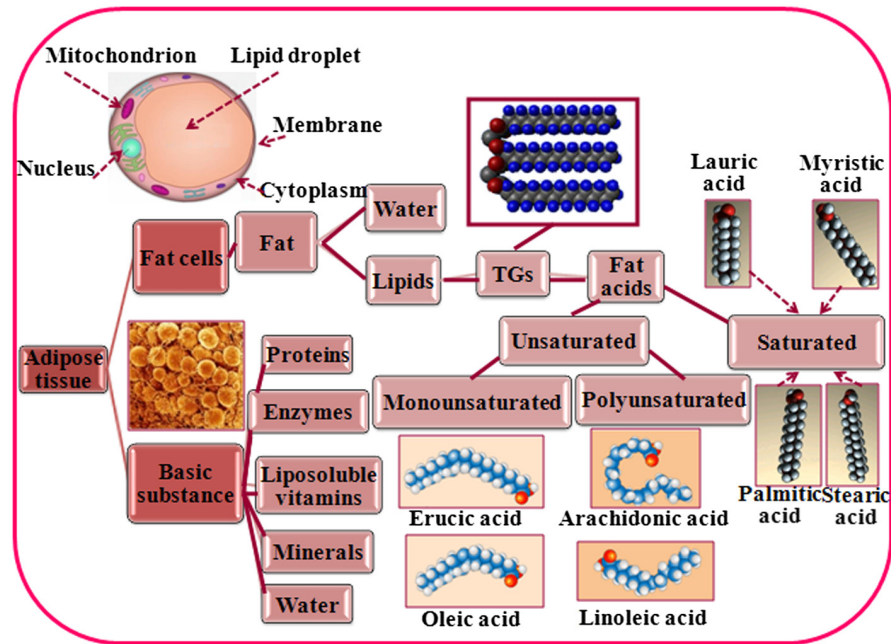


Fig. 1 Diagram of chemical and morphological composition of the AT. It is composed of adipocytes grouped in lobules separated by connective tissue. Approximately, 60% to 85% of the weight of white AT are lipids, with 90% to 99% being TGs.¹⁸ Small amounts of FFAs, diglycerides, cholesterol, phospholipids, and minute quantities of cholesterol esters and monoglycerides are also present. In this lipid mixture, six fatty acids make up ~90% of the total, and these are myristic, palmitic, palmitoleic, stearic, oleic, and linoleic. The remaining acids (erucic, arachidonic, and lauric) are less important. The diet can vary the fatty acid profile in AT. The remaining weight of white AT is composed of water (5% to 30%) and proteins (2% to 3%). The lipid droplet is structured as an organic core comprising neutral lipids bound to a monolayer of phospholipids.^{19,20} The neutral lipids are mainly TGs and sterol esters. Fatty acids are categorized according to the number and bonding of the carbon atoms in the aliphatic chain. Saturated fats have no double bonds between the carbon atoms in the chain, as unsaturated fats have one or more double bonded carbons in the chain. Atoms of hydrogen, carbon, and oxygen are represented by white, blue, and red spheres, respectively.

transition can be performed by measurements of the temperature dependence of the RI of the lipid-containing tissue components.

2.2 Optical Coherence Tomography and Abbe Refractometry

Structural changes in the tissue associated with the phase transitions can be assessed both *in vitro* and *in vivo* with OCT—a modern state-of-the-art noninvasive imaging modality.^{9,10,35,36} OCT is a well-known optical diagnostic technique to perform real-time 2-D and/or 3-D high-resolution (~5 to 8 μm) imaging of biological tissues *in vivo* with relatively high probing depth (up to 2 mm).^{37,38} Principles of this imaging modality are described in detail elsewhere.^{37–39} OCT has been extensively used for various applications in biomedical optics, including imaging of human skin, skin vessels, and skin blood circulation,^{40,41} connective tissue structure,⁴² individual vascular wall components⁴³ as well as for biotissue-mimicking phantoms,^{44,45} and noninvasive glucose sensing.^{46–48} Simultaneous measurements of the RI and thickness of the sample are the advantages of OCT compared with standard techniques.^{49–51}

In addition to OCT, the Abbe prism classical refractometry is an attractive tool for assessment of phase transitions in *in vitro* studies.^{52,53} For comparison of RI measurements performed by OCT and Abbe refractometry, it should be considered that due to a broadband light source used in OCT it measures the group RI of a material, as a single wavelength measurements of Abbe

refractometry give the phase RI. The group and phase RI are related; however, in dispersive media they are different. Simultaneous measurements of both phase and group RI and sample thickness are possible using combination of OCT and confocal microscopy⁵¹ or low-coherence interferometry at multiple angles of incidence enabling bulk RI measurement of scattering and soft samples.⁵⁴

Spectral-domain OCT has been extensively used to obtain subsurface images of ATs and for quantitative assessment of the RI.^{35,49–51} In the present study, we used a commercial OCT system (Hyperion, Thorlabs) operating at 930-nm central wavelength with a bandwidth of 100 nm for a high-resolution fat tissue imaging on the cellular level.

The experimental setup combining the OCT (Institute of Applied Physics RAS, Russia) and an Abbe refractometer (AR) DR-M2 1550 (Atago, Japan) to provide dual-mode concurrent measurements of RI temperature dependences is schematically shown in Fig. 2. In this setup, a time-domain OCT (5.8- μm axial, in air; 8- μm lateral) operating at a 910-nm central wavelength with a bandwidth of 49 nm was used for independent measurements of optical thickness of tissue samples, from which RI can be evaluated if the sample thickness is supposed to be constant during measurements.^{49–51} The optical thickness measured by OCT corresponds to the group RI multiplied by the physical thickness. However, due to a low dispersion of AT on the wavelength 910 nm within a bandwidth of 49 nm, the group RI is very close to the phase RI. This OCT system

Table 1 RI of different ATs.^{9,23-31}

AT type and body site	λ , nm	n , n_g (SD)	Method
Rat ²⁴	750 to 850	n_g : 1.467 (0.026)	OCT
Mesenteric in humans ²⁵	1300	n_g : 1.467 (0.008)	OCT
Abdominal in humans ^{9,26}	930	n_g : 1.460 (0.002)	OCT
		n_g : 1.386 (0.008)	
Subcutaneous in humans ²⁷	456 to 1064	1.44	Thin film reflectometry
Abdominal in humans ²⁷		1.46	
Bovine ²⁸	633	1.455 (0.006)	Fiber optic refractometry
Porcine ^{29,30}	488	1.510 (0.002)	Laser refractometry
	632.8	1.492 (0.003)	
	1079.5	1.482 (0.002)	
	1341.4	1.487 (0.004)	
Porcine ³¹	632.8	1.493 (0.005)	

Here n is the phase RI and n_g is the group RI. SD is standard deviation.

Table 2 The most common fatty acids of adipocytes.¹⁶

Structural formula	Name	Melting temperature, °C
Saturated fatty acids		
$\text{CH}_3(\text{CH}_2)_{10}\text{COOH}$	Lauric	44
$\text{CH}_3(\text{CH}_2)_{12}\text{COOH}$	Myristic	58
$\text{CH}_3(\text{CH}_2)_{14}\text{COOH}$	Palmitic	63
$\text{CH}_3(\text{CH}_2)_{16}\text{COOH}$	Stearic	70
$\text{CH}_3(\text{CH}_2)_{18}\text{COOH}$	Arachidic	77
Unsaturated fatty acids		
$\text{CH}_3(\text{CH}_2)_5\text{CH}=\text{CH}(\text{CH}_2)_7\text{COOH}$	Palmitoleic	-1
$\text{CH}_3(\text{CH}_2)_7\text{CH}=\text{CH}(\text{CH}_2)_7\text{COOH}$	Oleic	16
$\text{CH}_3(\text{CH}_2)_4(\text{CH}=\text{CHCH}_2)_2(\text{CH}_2)_6\text{COOH}$	Linoleic	-5
$\text{CH}_3\text{CH}_2(\text{CH}=\text{CHCH}_2)_3(\text{CH}_2)_6\text{COOH}$	Linolenic	-11
$\text{CH}_3(\text{CH}_2)_4(\text{CH}=\text{CHCH}_2)_4(\text{CH}_2)_2\text{COOH}$	Arachidonic	-49

Table 3 Approximate composition of porcine and human fats. FFA denotes the free fatty acids.

AT	Melting temperature, °C	FFA, % by mass (melting temperature, °C, from Table 1)				
		Palmitic	Stearic	Oleic	Linoleic	Linolenic
Porcine ³³	36 to 45	27 (63)	14 (70)	45 (16)	5 (-5)	5 (-11)
Visceral human ³⁴	30 to 35	25 (63)	8 (70)	46 (16)	10 (-5)	—

had a low spatial resolution; however, it was sufficient to provide RI measurements in different points of the samples and allowed to combine it with the AR.

For spectral-domain OCT measurements, tissue sample heating was managed by a homemade temperature control plate (based on thermoresistors) upon changing the externally applied voltage. The temperature was varied from room temperature (25°C) up to 70°C with the corresponding voltage changes in the range of 5 to 10 V. The data obtained were processed with MATLAB (MathWorks). In addition, a multiwavelength AR Atago equipped with a CMOS camera was used for the quantitative assessment of the RI, while the temperature was controlled in the range from the room temperature to 60°C by a thermostat T200 (GK Sondermaschinenbau, Germany) and was monitored remotely with an infrared camera FLIR b60 (FLIR, Sweden) providing 2% accuracy. The slices of ATs were placed on the prism of the AR.

AR employs the effect of total internal reflection to measure the RI n of a solid or liquid specimen in the visible or near-infrared (NIR) ranges. Traditionally, to obtain RIs of transparent specimens, the spatial distribution of transmitted light is analyzed.⁵⁵⁻⁵⁷ However, this method cannot be directly used for the measurement of RI of turbid biological tissues with strong scattering and absorption. Thus, in the current study, all the refractometric measurements were performed in the reflection mode.⁵⁸⁻⁶¹

The working principle of AR is based on the measurement of a critical angle. As it is shown in the inset of Fig. 2, the sample is placed on top of the measurement prism. A divergent light beam enters the sample through the prism, gets refracted at a critical angle on its surface, and then a telescope is used to measure position of the border between bright and dark areas. The telescope reverts the image, so the dark area is at the bottom, even if we expect it to be in the upper part of the field of view. Knowing the angle and RI of the measuring prism, it is not difficult to calculate RI of the sample⁶²

$$n = N \sin(i_{\text{crit}}), \tag{1}$$

where n and N are the RIs of the sample and the measuring prism, respectively.

Usually, the exiting angle of the critical beam from the prism to the air ϕ is measured. It is easy to show by considering the refraction of light beams on the face of the prism BC plane (Fig. 2) that the RI of the sample n is related to the angle ϕ

$$n = \sin B \sqrt{N^2 - \sin^2 \phi} - \cos B \sin \phi, \tag{2}$$

where B is the refracting angle of the prism (the angle between the refracting faces). In fact, when measuring, there is no need to

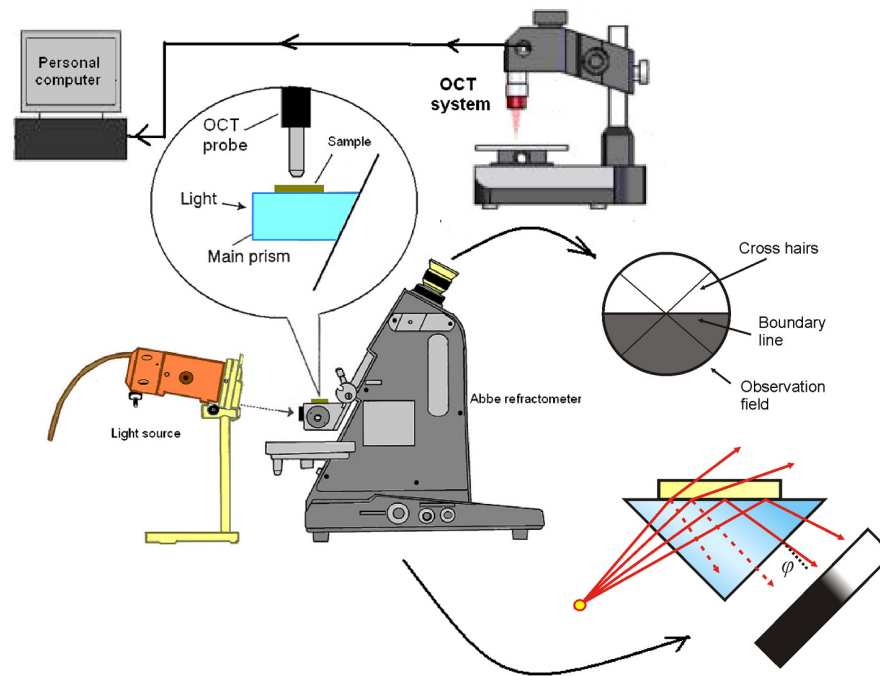


Fig. 2 Schematic illustration of combined optical coherence tomograph and Abbe refractometer system for assessing RI of AT samples. OCT system: spectral-domain (Hyperion, Thorlabs) or time-domain (Institute of Applied Physics RAS, Russia). Abbe refractometer: a multiwavelength refractometer Atago DR-M2 1550 (Atago, Japan); light source: JCR12V100W10H/G1/IR (Iwasaki, Japan); it also includes PixelLINK PL-B741F CMOS camera (detector size: 8.6 mm × 6.9 mm) (PixelLINK, Canada).

use this equation to calculate RIs, since the reference scale of the refractometer was calibrated in the values of n with regard to Eq. (2).

Calibration of the AR was carried out using 86%, 93%, and 100% glycerol–water solutions. RIs of the glycerol–water mixtures were calculated based on the corresponding data for the pure substances.⁶³ All the measurements were performed at the 930-nm wavelength using the corresponding optical filter (10-nm bandwidth) supplied with the refractometer. The images from the device fed into the CMOS camera comprise two sections: the brighter part (Fig. 3) formed by light beams totally reflected from the sample, and the dark part formed by rays only partially reflected from the sample (and partially transmitted through it).

The recorded images were processed using the ImageJ software: normalization to the background and retrieval of the profile intensity curves across the screen perpendicular to the shadow-light interface [Fig. 4(a)]. The resulting calibration curve [Fig. 4(b)] shows dependence of the RI on the screen coordinate.

Fresh samples of porcine AT from food market were used in the studies. Experiments were performed for 30 samples taken from the same piece of porcine AT (10 samples were used for each series of experiments). Slicing of frozen AT samples was carried out manually with a scalpel. About 1- to 2-mm-thick tissue slices were heated from the room temperature up to 60°C by running water from a thermostat and corresponding refractometer images were automatically recorded by the CMOS camera. The RIs were retrieved during postprocessing of the obtained images: location of the light-shadow border was associated with the X -coordinate [Fig. 4(a)], and the corresponding RI was found using the calibration curve [Fig. 4(b)].

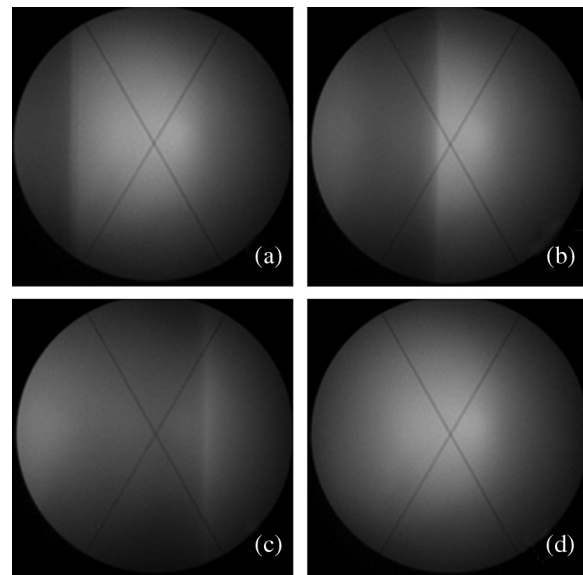


Fig. 3 Refractometer screen images (used for calibration) upon application of aqueous solutions of glycerol of different concentrations: (a) 86%, (b) 93%, (c) 100%, and (d) background.

Statistical analysis of data was performed using the Statistics 6.0 software.

3 Results and Discussion

Figure 5 and Video 1 (see supplement) show the temporal evolution of OCT images of porcine fat with temperature increase from 23°C to 70°C. On high-resolution OCT images, well-seen

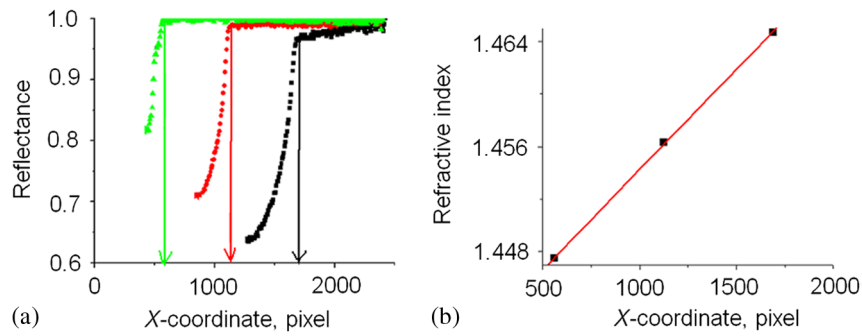


Fig. 4 (a) Profile intensity curves obtained from three glycerol-water solutions (black square—100%, $n = 1.4641$; red circle—93%, $n = 1.4554$; green triangle—86%, $n = 1.4466$) and (b) the resulting calibration curve. The vertical arrows in (a) indicate the border between dark (to the left of the lines) and light (to the right) areas and the intersection positions (in pixels) with the X-axis correspond to refractive indices of the relevant water-glycerol solutions. The calibration did not go beyond the accuracy of the measurements provided by the Atago refractometer (10^{-4}).

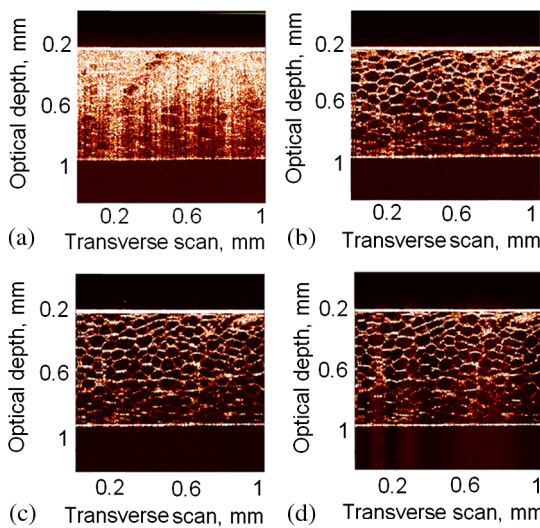


Fig 5 OCT images of AT samples at different temperatures: (a) 23°C, (b) 35°C, (c) 45°C, and (d) 55°C. The Video 1 file shows kinetics of the OCT images alterations (Video 1, MP4, 2.16 MB [URL: <http://dx.doi.org/10.1117/1.JBO.23.1.016003.1>]).

temperature-induced fat tissue optical clearing on the cellular level happened due to reduction in the light scattering. This reduction was caused by the phase transition of lipids localized in droplets from crystalline to liquid state for temperatures from about 35°C.

OCT provides accurate measurements of the RI with the approximate precision of 1% if the geometrical thickness is known. The effective RI of the tissue sample was assessed as the ratio^{36,37}

$$n = \frac{z}{l}, \quad (3)$$

where l is the geometrical (true) thickness of the sample and z is the OCT-observed depth, i.e., the optical thickness.

The RI of AT was assessed for the optical thickness of samples obtained with spectral- or time-domain OCT systems. The optical thickness was found from the A-scan of the OCT images as a distance between two main peaks associated with the sample-glass interfaces. To provide better localization

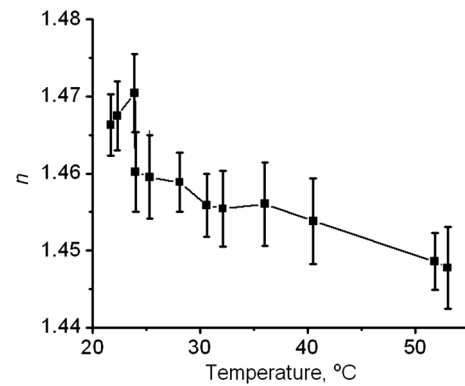


Fig. 6 Temperature dependence of the RI of AT obtained by OCT measurements. Bars show SDs and the line connecting mean values of RI shows local alterations of the slope of RI temperature dependence.

of the boundaries, the A-scans were averaged over a certain lateral region (2 mm). This operation smooths out the random noise in the system and influence of inhomogeneity of cell structure of the tissue, while the peaks corresponding to the sample boundaries become more distinct.^{9,10} Processing and smoothing of OCT signals and determination of distance between peaks were performed using MathCAD (PTC, Inc.). The “medsmooth” function was used for smoothing with the help of a sliding median.

Figure 6 shows the temperature dependence of the RI of AT samples reconstructed from the OCT images (Fig. 5).

At the same time, 10 samples of AT *in vitro* were studied using Atago AR and the time-domain OCT. The heating time of each sample was in the range of 4 to 10 min. The results obtained using the described procedure are shown in Fig. 7, from which RI values were retrieved.

The resulting changes of the relative slope of the RI and the phase transitions of the main components of lipids in AT in response to the temperature increase are shown in Fig. 8. The phase transition is defined as a change in the relative slope of the temperature dependence of the RI. The temperature of tissue samples in that case was recorded remotely and analyzed in real time by a thermal imaging camera FLIR b60. This camera allows for distant temperature measurements in the range from -20°C to 120°C with accuracy better than 0.1°C.⁶⁴

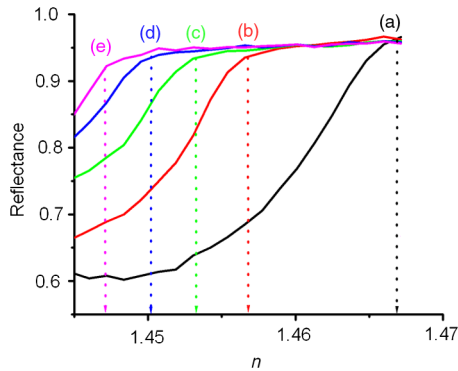


Fig. 7 Reflectance retrieved from the measurements with the Abbe refractometer for different temperatures in the course of temperature elevation: (a) 0 s, 21.9°C; (b) 180 s, 30.4°C; (c) 285 s, 40.7°C; (d) 375 s, 49.4°C; and (e) 435 s, 56.1°C. The arrows indicate estimated values of the RI for the relevant temperature.

Table 4 shows mean value and SD of phase transition characteristic temperatures averaged over 10 fat samples studied by each measurement technique [AR, spectral OCT (S-OCT), and AR/time-domain OCT (AR/TD-OCT)] and comparison with the independent measurements done for 10 samples using optoacoustic technique.^{65,66}

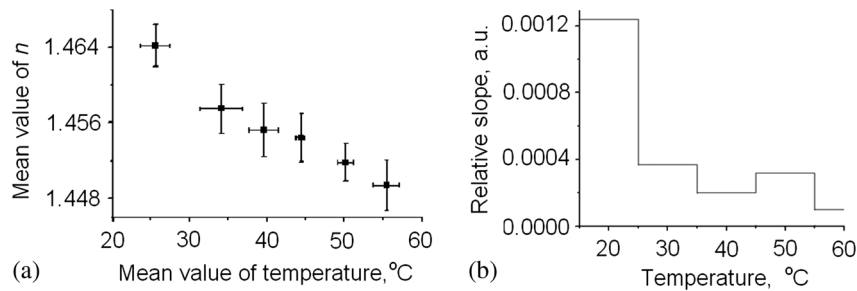


Fig. 8 Phase transition characteristics of AT samples: (a) averaged data for phase transition temperatures for 10 studied samples (Table 4) and (b) the phase transition is defined as a change in the relative slope of the temperature dependence of the RI. Bars show SDs.

Table 4 Mean values and SD of phase transition temperatures found for studied 30 fat samples using AR, spectral OCT (S-OCT), AR/time-domain OCT (AR/TD-OCT), and OA technique (10 fat samples).^{65,66} *N* is the number of samples for which a particular phase transition was observed.

Transition	Phase transition temperature (mean ± SD)°C						
	AR (Fig. 8)	<i>N</i>	S-OCT (Fig. 6)	<i>N</i>	AR/TD-OCT (Fig. 9)	<i>N</i>	OA ^{65,66}
Very-low-temperature	—	—	24.0 ± 1.7	10	22.3 ± 2.6	10	—
	25.5 ± 1.9	9	26.5 ± 3	10	25.3 ± 3	10	26 ± 2
Low-temperature	—	—	32.5 ± 2.5	9	30.6 ± 2	8	—
	34.1 ± 2.8	10	35.2 ± 1.5	9	—	—	35 ± 2
Middle-temperature	39.5 ± 1.9	9	—	—	—	—	42 ± 2
	44.4 ± 0.6	6	—	—	—	—	—
High-temperature	50.2 ± 1.0	6	—	—	50.3 ± 3	8	—
	55.5 ± 1.6	5	53.5 ± 2.6	8	—	—	52 ± 2
	—	—	—	—	—	—	65 ± 2

It is worth noting that data presented in Table 4 for all 30 samples studied in this paper demonstrate existence of the very-low-temperature transitions for 29 samples in the range from 22.3°C to 26.5°C detected by all three measurement techniques (AR, S-OCT, and AR/TD-OCT, respectively). The low-temperature transitions in the range from 30.6°C to 35.2°C were also detected by all techniques for 27 samples, whereas the middle-temperature range transitions between (39.5 ± 1.9)°C and (44.4 ± 0.6)°C were found only for AR measurements, for nine and six samples from studied 10, respectively. The high-temperature transitions, which are in the range from 50.2°C to 55.5°C, were detected for 22 samples by all three measurement techniques.

It also should be pointed out that temperature dependence observed with concurrent dual modal technique [refractometry and OCT (Fig. 9)] agrees well with the results obtained by optoacoustic measurements for *ex vivo* samples of porcine fat (the right column of Table 4).^{65,66} Data received for both techniques have a similar trend and high correlation index (Spearman's rank correlation coefficient between the OCT and the optoacoustic measurements was 0.958; between the refractometry and the optoacoustic measurements was 0.958). Unfortunately, we could not compare the second high-temperature transition of porcine fat found in optoacoustic measurements at (65 ± 2)°C

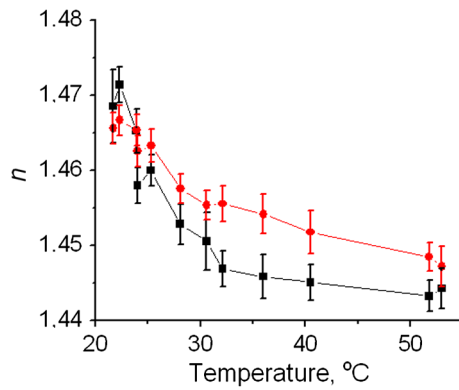


Fig. 9 Temperature dependence of the RI of AT obtained by the time-domain OCT (black square) and the Abbe refractometer (red circle) concurrent measurements. Bars show SDs.

because of a limited working temperature range of the Atago refractometer.

The low-temperature phase transitions (22°C to 35°C) could be associated with the fusible FFA of the fat droplet like oleic acid; the middle-temperature (40°C to 44°C)—with cell membrane phospholipids, and the high-temperature (45°C to 55°C)—with less fusible FFT of the fat droplet, such as palmitic acid.

The temperature dependence of RI can be described as^{67,68}

$$n = n_0 + (dn/dT)T, \quad (4)$$

where T is temperature [°C].

For our data (see Fig. 8), the averaged RI temperature increment dn/dT equals to $[-(5.3 \pm 0.6)] \times 10^{-4} \text{°C}^{-1}$ with $n_0 = 1.466$ corresponding well to the increment measured for the oleic acid,^{16–20} $[-3.8 \times 10^{-4} \text{°C}^{-1}]$ (as shown in Ref. 68) with $n_0 = 1.467$. This result can be explained by the high content of oleic acid in porcine fat (45%) and its low melting temperature (16°C) (Table 3). Therefore, it easily and intensively leaks out from the adipose cells and accumulates on the interface between the sample and the refractometer measuring prism.

Figure 9 shows temperature dependence of the RI of AT sample calculated from the A -scans of OCT images and concurrently measured using the refractometer. As one can see, the RI data retrieved by the two independent methods are in good agreement with each other and show the similar trend (Spearman's rank correlation coefficient was 0.99). However, the inhomogeneity mostly caused by a nonuniform distribution of the temperature within the sample under study and its individual properties affect evaluation of the phase transition temperatures manifested as an error (SD) (see Fig. 9 and Table 4).

The phase transitions of lipids' components of the AT correspond to changes of the RI temperature slope (see Fig. 8). According to the literature data, porcine fat undergoes such phase transitions within the temperature range of 36°C to 45°C.³³ The obtained results are in good agreement with the data presented in Table 3, which are related to phase transitions of lipids in the adipocyte lipid droplet. The temperature variations of RI associated with phase transitions of phospholipid bilayer of cell membranes found for extracted membranes from the animal tissue studied by OCT are in the temperature range 38°C to 42°C.³⁵ In its turn, differential scanning calorimetry measurements for fat tissue indicated broad endothermic transitions centered near 60°C to 65°C, closely matching the

transition temperature reported for stratum corneum lipid extracts.^{6,69,70} Therefore, we can suppose that the revealed multiple phase transitions are attributed to lipids in the fat cell droplet and phospholipids in the cell membrane.

4 Summary and Conclusions

In the study, the temperature dependences of RI of the AT have been observed by application of a combined OCT and conventional Abbe refractometry approach. The melting phase transitions were quantified and associated with corresponding transitions of lipids in fat droplets and phospholipids in the adipocyte membranes. The results obtained for RI measurements by spectral OCT, time-domain OCT, and Abbe refractometry are in good agreement with each other both qualitatively and quantitatively. OCT measurements of phase transitions are prospective for *in vivo* studies and can be routinely used to assess the temperature-induced RI change of fat cells near the skin surface. It is important to note that phase transitions of lipids inside lipid droplets can be also detected by OCT via monitoring of reduction of light scattering (cellular optical clearing).

The presented approach has a high potential to be used for getting more valuable information about processes taking place during thermally induced fat cell lipolysis for more accurate quantification of many different therapeutic protocols, including laser therapy for body contouring and spot fat reduction and photochemotherapy of cancer patients.

Disclosures

No conflicts of interest, financial or otherwise, are declared by the authors.

Acknowledgments

The authors thank Dr. S. V. Eremina (Department of English and Intercultural Communication of Saratov State University) for proof of English, L.E. Dolotov for help in design of the registration part of the AR Atago DR-M2 1550 (Atago, Japan). This study was supported in part by Academy of Finland projects Grants 288164 (I.Yu.Y.), 260321 and 290596 (A.P.P., A.V.B.); the Russian Presidential Grant Nos. MK-6009.2016.2 (I.Yu.Y.) and NSh-7898.2016.2 (V.V.T. and I.Yu.Y.), the Government of Russian Federation Grant No. 074-U01 (A.P.P., A.V.B., I.V.M., and V.V.T.), and the Tomsk State University Competitiveness Improvement Programme (I.Yu.Y. and V.V.T.). I.V.M. also acknowledges a partial support provided by the Russian Science Foundation project No. 15-14-10008. All authors have no financial interest.

References

1. J. Langerhoic, "Moving phase transitions in laser-irradiated biological tissue," *Appl. Opt.* **18**(13), 2286–2293 (1979).
2. J. Zhou, J. Liu, and A. Yu, "Numerical study on the thawing process of biological tissue induced by laser irradiation," *J. Biomech. Eng.* **127**(3), 416–431 (2005).
3. J. Zhou, J. K. Chen, and Y. Zhang, "Theoretical analysis of thermal damage in biological tissues caused by laser irradiation," *Mol. Cell. Biomech.* **4**(1), 27–39 (2007).
4. A. Vogel and V. Venugopalan, "Pulsed laser ablation of soft biological tissues," in *Optical-Thermal Response of Laser-Irradiated Tissue*, A. J. Welch and M. J. C. van Gemert, Eds., pp. 551–615, Springer, Dordrecht (2011).
5. D. Deepa, *Laser Assisted Breast Tumor Excision under MRI Guidance: A Multi-Variate Study*, University of Minnesota, ProQuest Dissertations Publishing, 3373386 (2009).

6. V. N. Bagratashvili et al., "Structural changes in connective tissues caused by a moderate laser heating," *Quantum Electron.* **32**(10), 913–916 (2002).
7. A. V. Belikov, C. V. Prikhodko, and O. A. Smolyanskaya, "Study of thermo-induced changes resulted in optical properties of fat tissue," *Proc. SPIE* **5066**, 207 (2003).
8. G. V. Simonenko et al., "Thermal action on the lipocells," *Proc. SPIE* **5068**, 458 (2003).
9. I. Y. Yanina, N. A. Trunina, and V. V. Tuchin, "Optical coherence tomography of adipose tissue at photodynamic/photothermal treatment in vitro," *J. Innovative Opt. Health Sci.* **6**(2), 1350010 (2013).
10. I. Y. Yanina, N. A. Trunina, and V. V. Tuchin, "Photoinduced cell morphology alterations quantified within adipose tissues by spectral optical coherence tomography," *J. Biomed. Opt.* **18**(11), 111407 (2013).
11. G. B. Altshuler et al., "Extended theory of selective photothermolysis," *Lasers Surg. Med.* **29**, 416–432 (2001).
12. M. Wanner et al., "Effects of non-invasive, 1,210 nm laser exposure on adipose tissue: results of a human pilot study," *Lasers Surg. Med.* **41**, 401–407 (2009).
13. B. R. Seckel et al., "The role of laser tunnels in laser-assisted lipolysis," *Lasers Surg. Med.* **41**(10), 728–737 (2009).
14. P. Avci et al., "Low-level laser therapy for fat layer reduction: a comprehensive review," *Lasers Surg. Med.* **45**(6), 349–357 (2013).
15. M. K. Caruso-Davis et al., "Efficacy of low-level laser therapy for body contouring and spot fat reduction," *Obes. Surg.* **21**(6), 722–729 (2011).
16. S. Ojha, H. Budge, and M. E. Symonds, "Adipocytes in normal tissue biology," in *Pathobiology of Human Disease. A Dynamic Encyclopedia of Disease Mechanisms, Part II: Organ Systems Pathophysiology*, L. M. McManus and R. N. Mitchell, Eds., pp. 2003–2013, Academic Press, San Diego (2014).
17. M. C. Michalski et al., "Multiscale structures of lipids in foods as parameters affecting fatty acid bioavailability and lipid metabolism," *Prog. Lipid Res.* **52**(4), 354–373 (2013).
18. A. L. Albright and J. S. Stern, "Adipose tissue," in *Encyclopedia of Sports Medicine and Science*, T. D. Fahey, Ed., <http://www.sportsmedicine.com/encycl> (1998).
19. Y. Guo et al., "Lipid droplets at a glance," *J. Cell Sci.* **122**(6), 749–752 (2009).
20. T. Fujimoto and R. G. Parton, "Not just fat: the structure and function of the lipid droplet," *Cold Spring Harbor Perspect. Biol.* **3**, a004838 (2011).
21. B. Cletus et al., "Temperature-dependent optical properties of Intralipid® measured with frequency-domain photon-migration spectroscopy," *J. Biomed. Opt.* **15**(1) 017003 (2010).
22. I. Y. Yanina et al., "Monitoring of temperature-mediated adipose tissue phase transitions by refractive-index measurements," *Proc. SPIE* **9421** 94210K (2014).
23. V. V. Tuchin, *Tissue Optics: Light Scattering Methods and Instruments for Medical Diagnostics*, 3rd ed., SPIE Press, Bellingham, Washington (2015).
24. A. M. Zysk et al., "Refractive index of carcinogen-induced rat mammary tumors," *Phys. Med. Biol.* **51**, 2165–2177 (2006).
25. G. J. Tearney et al., "Determination of the refractive index of highly scattering human tissue by optical coherence tomography," *Opt. Lett.* **20**, 2258–2260 (1995).
26. I. Y. Yanina, N. A. Trunina, and V. V. Tuchin, "Temporal change of adipose tissue refractive index at photodynamic treatment: in vitro study using OCT," *Proc. SPIE* **8222**, 82221G (2012).
27. A. Roggan et al., "The optical properties of biological tissue in the near infrared wavelength range—review and measurements," in *Laser-Induced Interstitial Thermotherapy*, G. Muller and A. Roggan, Eds., pp. 10–44, SPIE Press, Bellingham, Washington (1995).
28. F. P. Bolin et al., "Refractive index of some mammalian tissues using a fiber optic cladding method," *Appl. Opt.* **28**, 2297–2303 (1989).
29. S. Cheng et al., "Measurement of the refractive index of biotissue at four laser wavelengths," *Proc. SPIE* **4916**, 172–176 (2002).
30. Q. Ye et al., "Measurement of the complex refractive index of tissue-mimicking phantoms and biotissue by extended differential total reflection method," *J. Biomed. Opt.* **16**(9), 097001 (2011).
31. H. Liu and S. Xie, "Measurement method of the refractive index of biotissue by total internal reflection," *Appl. Opt.* **35**, 1793–1795 (1996).
32. M. A. F. Domingues et al., "Advances in lipids crystallization technology," Chapter 5 in *Advanced Topics in Crystallization*, Y. Mastai, Ed., pp. 105–132, InTech, Rijeka (2015).
33. S. N. Turk and S. B. Smith, "Carcass fatty acid mapping," *Meat Sci.* **81**, 658–663 (2009).
34. S. Schmidt-Nielsen, "Melting points of human fats as related to their location in the body," *Acta Physiol.* **12**(2–3), 123–129 (1946).
35. M. Haruna et al., "Detection of phase transition of a biological membrane by precise refractive-index measurement based on the low coherence interferometry," *Proc. SPIE* **3915**, 188–193 (2000).
36. A. Knüttel, S. Bonev, and W. Knaak, "New method for evaluation of in vivo scattering and refractive index properties obtained with optical coherence tomography," *J. Biomed. Opt.* **9**(2), 265–273 (2004).
37. B. E. Bouma and C. J. Tearney, *Handbook of Optical Coherence Tomography*, Marcel Dekker, Inc., New York (2002).
38. V. V. Tuchin, Ed., *Coherent-Domain Optical Methods: Biomedical Diagnostics, Environmental Monitoring and Material Science. V.1-2*, 2nd ed., Springer-Verlag, Berlin, Heidelberg, New York (2012).
39. W. Drexler and J. G. Fujimoto, Eds., *Optical Coherence Tomography. Technology and Applications*, 2nd ed., Springer-Verlag, Berlin, Heidelberg (2015).
40. J. Enfield, E. Jonathan, and M. Leahy, "In vivo imaging of the micro-circulation of the volar forearm using correlation mapping optical coherence tomography (cmOCT)," *Biomed. Opt. Express* **2**(5), 1184–1193 (2011).
41. A. Doronin and I. Meglinski, "Imaging of subcutaneous microcirculation vascular network by double correlation optical coherence tomography," *Laser Photonics Rev.* **7**(5), 797–800 (2013).
42. A. Bykov et al., "Imaging of subchondral bone by optical coherence tomography upon optical clearing of articular cartilage," *J. Biophotonics*, **9**(3), 270–275 (2016).
43. F. J. van der Meer et al., "Temperature dependent optical properties of individual vascular wall components, measured by optical coherence tomography," *J. Biomed. Opt.* **11**, 041120 (2006).
44. A. V. Bykov et al., "Multilayer tissue phantoms with embedded capillary system for OCT and DOCT imaging," *Proc. SPIE* **80911**, 80911R (2011).
45. R. V. Kuranov et al., "Depth-resolved blood oxygen saturation measurement by dual-wavelength photothermal (DWP) optical coherence tomography," *Biomed Opt. Express*, **2**(3), 491–504 (2011).
46. K. V. Larin et al., "Noninvasive blood glucose monitoring with optical coherence tomography—a pilot study in human subjects," *Diabetes Care* **25**, 2263–2267 (2002).
47. A. P. Popov et al., "Glucose sensing in flowing blood and intralipid by laser pulse time-of-flight and optical coherence tomography techniques," *IEEE J. Sel. Top. Quantum* **18**(4), 1335–1342 (2012).
48. E. Alarousu et al., "Noninvasive glucose sensing in scattering media using OCT, PAS, and TOF techniques," *Proc. SPIE* **5474**, 33–41 (2004).
49. X. Wang et al., "Simultaneous refractive index and thickness measurements of biotissue by optical coherence tomography," *J. Biomed. Opt.* **7**(4), 628–632 (2002).
50. P. H. Tomlins and R. K. Wang, "Simultaneous analysis of refractive index and physical thickness by Fourier domain optical coherence tomography," *IEEE Proc.-Optoelectron.* **153**(5), 222–228 (2006).
51. S. Kim et al., "Simultaneous measurement of refractive index and thickness by combining low-coherence interferometry and confocal optics," *Opt. Express* **16**, 5516–5526 (2008).
52. A. García-Valenzuela and H. Contreras-Tello, "Optical model enabling the use of Abbe-type refractometers on turbid suspensions," *Opt. Lett.* **38**(5), 775–777 (2013).
53. H. Contreras-Tello and A. García-Valenzuela, "Refractive index measurement of turbid media by transmission of backscattered light near the critical angle," *Appl. Opt.* **53**(21), 4768–4778 (2014).
54. P. H. Tomlins et al., "Optical coherence refractometry," *Opt. Lett.* **33**, 2272–2274 (2008).
55. G. H. Meeten and A. N. North, "Refractive index measurement of turbid colloid fluids by transmission near the critical angle," *Meas. Sci. Technol.* **2**, 441–447 (1991).
56. J. Rheims, J. Kosery, and T. Wriedt, "Refractive-index measurements in the near-IR using an Abbe refractometer," *Meas. Sci. Technol.* **8**, 601–605 (1997).

57. H. Contreras-Tello et al., "Understanding the performance of Abbe-type refractometers with optically absorbing fluids," *Meas. Sci. Technol.* **25**, 075201 (2014).
58. J. Lai et al., "Experimental measurement of the refractive index of biological tissues by total internal reflection," *Appl. Opt.* **44**, 1845–1849 (2005).
59. G. H. Meeten and A. North, "Refractive index measurement of absorbing and turbid fluids by reflection near the critical angle," *Meas. Sci. Technol.* **6**, 214–221 (1995).
60. G. Morales-Luna et al., "Experimental test of reflectivity formulas for turbid colloids: beyond the Fresnel reflection amplitudes," *J. Phys. Chem. B* **120**, 583–595 (2016).
61. Q. Ye et al., "Measurement of the complex refractive index of tissue-mimicking phantoms and biotissue by extended differential total reflection method," *J. Biomed. Opt.* **16**(9), 097001 (2011).
62. <http://www.refractometer.pl/Abbe-refractometer> (09 November 2017).
63. www.refractiveindex.info (09 November 2017).
64. <http://www.merlinlazer.com/b60-Infrared-Thermal-Imaging-Camera-2> (09 November 2017).
65. S. M. Nikitin, T. D. Khokhlova, and I. M. Pelivanov, "Measurement of the temperature dependence of the efficiency of optoacoustic conversion in tissues in-vitro," *Quantum Electron.* **42**(3), 269–278 (2012).
66. S. M. Nikitin, T. D. Khokhlova, and I. M. Pelivanov, "Temperature dependence of the optoacoustic transformation efficiency in ex-vivo tissues for application in monitoring thermal therapies," *J. Biomed. Opt.* **17**, 061214 (2012).
67. G. Bernardo-Gil, M. Esquivel, and A. Ribeiro, "Densities and refractive indices of pure organic acids as a function of temperature," *J. Chem. Eng. Data* **35**(2), 202–204 (1990).
68. F. Ferreira de Sousa et al., "Dielectric properties of oleic acid in liquid phase," *J. Bionanosci.* **3**, 139–142 (2010).
69. G. M. Golden et al., "Lipid thermotropic transitions in human stratum corneum," *J. Invest. Dermatol.* **86**(3), 255–259 (1986).
70. G. M. Golden et al., "Stratum corneum lipid phase transitions and water barrier properties," *Biochemistry* **26**(8), 2382–2388 (1987).

Irina Y. Yanina received her PhD in biophysics from Saratov State University (SSU), Saratov, Russia, in 2013. She is authored 17 papers in peer-reviewed journals and 18 papers in conference proceedings. From 2010 to present, she is an associate fellow researcher of Laboratory of Biomedical Optics of Research-Educational Institute of Optics and Biophotonics at SSU. Her research interests include the development of optical methods of fat tissue destructive engineering, photodynamic/photothermal therapy, biomedical optics, drug delivery,

spectroscopy and imaging in biomedicine, optical and laser measurements.

Alexey P. Popov graduated with honors from Physics Department of M.V. Lomonosov Moscow State University (MSU), Russia, in 2003, received his PhD from MSU in 2006 and his DSc (Tech.) degree from the University of Oulu, Finland, in 2008. He is currently an adjunct professor at the University of Oulu. His scientific interests are in the area of nanobiophotonics, light-biotissue interaction, optical imaging and sensing, design of biotissue-mimicking phantoms. He published over 100 journal papers and peer-reviewed conference proceedings; organized such international conferences as Advanced Laser Technologies ALT-2007 (Levi, Finland), Laser Applications in Life Sciences LALS-2010 (Oulu, Finland), Summer SPIE FOCUS School on Optics and Photonics 2017 (Oulu, Finland). He served as a guest editor of the *Journal of Biophotonics* (Special Issue devoted to the LALS-2010 conference). He is a SPIE senior member, a SPIE student chapter faculty advisor, and an OSA member.

Alexander V. Bykov is a senior research fellow/adjunct professor in the Optoelectronics and Measurement Techniques Unit, University of Oulu, Finland. He received his PhD in 2008 from Lomonosov Moscow State University, Russia and DSc (Tech.) degree in 2010 from the Faculty of Technology, University of Oulu, Finland. He is an author and coauthor of over 80 papers in peer-reviewed scientific journals, international conference proceedings and book chapters.

Igor V. Meglinski is a professor at the Opto-Electronics and Measurement Techniques Research Unit, University of Oulu (Finland). His research interests include propagation of coherent polarized light in turbid tissue-like scattering media, coherent effects of multiple scattering of light, tissue polarimetry, angular momentum of light, optical phase singularities, dynamic light scattering, Monte Carlo modelling and multimodal imaging. He is chartered physicist (CPhys), fellow of the Institute of Physics (London, UK), senior member of IEEE, and fellow of SPIE.

Valery V. Tuchin is a professor and head of optics and biophotonics at Saratov State University (National Research University of Russia) and several other universities. His research interests include tissue optics, laser medicine, tissue optical clearing, and nanobiophotonics. He is a fellow of SPIE and OSA, has been awarded Honored Science Worker of the Russia, Honored Professor of Saratov University, SPIE Educator Award, FiDiPro (Finland), Chime Bell Prize of Hubei Province (China), NanQiang Life Science Series Lectures Award of Xiamen University (China), and Joseph W. Goodman Book Writing Award (OSA/SPIE).